

PAPER • OPEN ACCESS

Dynamics of an impurity in a one-dimensional lattice

To cite this article: F Massel *et al* 2013 *New J. Phys.* **15** 045018

View the [article online](#) for updates and enhancements.

You may also like

- [ALMA Spatially Resolved Dense Molecular Gas Survey of Nearby Ultraluminous Infrared Galaxies](#)
Masatoshi Imanishi, , Kouichiro Nakanishi et al.
- [Deeply Buried Nuclei in the Infrared-luminous Galaxies NGC 4418 and Arp 220. II. Line Forests at \$\lambda = 1.4\text{--}0.4\text{ mm}\$ and Circumnuclear Gas Observed with ALMA](#)
Kazushi Sakamoto, Sergio Martín, David J. Wilner et al.
- [The Molecular Interstellar Medium in the Super Star Clusters of the Starburst NGC 253](#)
Nico Krieger, Alberto D. Bolatto, Adam K. Leroy et al.

Dynamics of an impurity in a one-dimensional lattice

F Massel^{1,5,6}, A Kantian², A J Daley³, T Giamarchi² and P Törmä⁴

¹ Olli V Lounasmaa Laboratory, Aalto University, FI-00076 Aalto, Finland

² DPMC-MaNEP, University of Geneva, 24 Quai Ernest Ansermet, 1211 Geneva, Switzerland

³ Department of Physics and Astronomy, University of Pittsburgh, Pittsburgh, PA 15213, USA

⁴ COMP Centre of Excellence, Department of Applied Physics, Aalto University, FI-00076 Aalto, Finland

E-mail: francesco.massel@helsinki.fi

New Journal of Physics **15** (2013) 045018 (25pp)

Received 12 October 2012

Published 23 April 2013

Online at <http://www.njp.org/>

doi:10.1088/1367-2630/15/4/045018

Abstract. We study the non-equilibrium dynamics of an impurity in a harmonic trap that is kicked with a well-defined quasi-momentum, and interacts with a bath of free fermions or interacting bosons in a one-dimensional lattice configuration. Using numerical and analytical techniques we investigate the full dynamics beyond linear response, which allows us to quantitatively characterize states of the impurity in the bath for different parameter regimes. These vary from a tightly bound molecular state in a strongly interacting limit to a polaron (dressed impurity) and a free particle for weak interactions, with composite behaviour in the intermediate regime. These dynamics and different parameter regimes should be readily realizable in systems of cold atoms in optical lattices.

⁵ Present address: Department of Mathematics and Statistics, University of Helsinki, PO Box 68, FI-00014 Helsinki, Finland.

⁶ Author to whom any correspondence should be addressed.



Content from this work may be used under the terms of the [Creative Commons Attribution-NonCommercial-ShareAlike 3.0 licence](https://creativecommons.org/licenses/by-nc-sa/3.0/). Any further distribution of this work must maintain attribution to the author(s) and the title of the work, journal citation and DOI.

Contents

1. The fermionic system	4
1.1. The basic model and method	4
1.2. The non-interacting impurity	4
2. Dynamics of an impurity in a fermionic bath	5
2.1. Strong interactions: the low-frequency peak	8
2.2. Strong interactions: the high-frequency peak	11
2.3. Weak interactions	16
2.4. Damping	17
3. The kicked impurity in a bosonic reservoir	17
3.1. The weak interaction limit	17
3.2. The strong interaction limit—higher-order bound states of the impurity	19
4. Discussion and conclusions	20
Acknowledgments	21
Appendix	21
References	24

Impurities play a crucial role in determining the low-temperature features of a number of condensed matter systems. These impurities may be localized ones, as for the x-ray edge [1] and Kondo effects [2], or mobile ones, like the itinerant single electrons modified by the phonon bath of the solid-state crystal in which they move (polarons) [1], or the single spin-flipped electron moving in a lattice populated by opposite spin electrons, as studied in the context of high- T_c superconductors [3]. With the recent experimental developments on systems of ultracold atoms, such as the tunability of the two-body interaction with the aid of Feshbach resonances [4], a particularly well-controlled environment [5] to explore the properties of these types of many-body systems has become available.

For two- and three-dimensional (3D) systems, these advances have enabled the experimental [6–11] and theoretical [12–23] study of mobile impurities inside a fermionic bath, i.e. a type of polaron, usually created by preparing two-component ultracold Fermi gases with a large number imbalance between the components. In this context, the possibility of tuning the bath–impurity interaction across a wide range and even from attractive to repulsive regimes has opened up both the polaronic and the molecular regime to investigations. These advances have also stirred interest in using these fermionic systems to study the dynamics of the x-ray edge effect, which is induced by a localized impurity [23].

At the same time, the ability to restrict the spatial dimension of ultracold gas experiments almost arbitrarily has also made possible the study of impurities inside one-dimensional (1D) many-body baths. As the movement of the impurity in such a bath can very easily involve the collective motion of many bath atoms, the result can be profoundly modified compared with what would be expected in higher-dimensional systems, giving rise to a regime of subdiffusive impurity motion, in which it can displace only proportional to the logarithm of time, more slowly than any power law [24–28]. Another reason for the particular interest in 1D impurity–bath systems is that they make particularly compelling benchmark systems for a wide range of

impurity–bath systems, due to the powerful theoretical approaches available to treat interacting 1D systems [29, 30]. For example, the ground state of an impurity in a 1D Fermi gas in a lattice was calculated via exact numerical methods [31], demonstrating that it can be described by a polaron-type ansatz for weak interactions, while the strong-interaction regime corresponds well to the strongly interacting limit of the Bethe ansatz. Static properties of polarons in 1D ultracold Fermi gases have been studied also in [32], and in recent years there has been interest in exploring the dynamics as well [33, 34]. Complementary to the fermionic case, the dynamics of an impurity in a continuous bosonic bath was recently studied experimentally and theoretically [35–38]. Major advances with single-site addressing and manipulation in optical lattices [39, 40] have recently enabled the realization of lattice impurities within a bath described by a 1D Bose–Hubbard model [41].

In this paper, we explore the basic dynamical properties of a single impurity in a lattice potential and a harmonic trap in 1D, which interacts with a bath of free fermions or interacting bosons, also confined in the 1D lattice. Specifically, we consider the non-equilibrium response of the impurity to a kick with well-defined momentum. A key open question in this context is how to characterize the role that the bath atoms play in the dynamics. In particular, we ask whether the dynamical response of the system implies polaronic behaviour, in which the properties of the particle are renormalized by the presence of the bath, or whether the interaction gives rise to other states, e.g. to tightly bound pairs or more complex objects.

Using time-evolving block decimation (TEBD) methods [42–45] in conjunction with the Bethe-ansatz results, we study the non-equilibrium dynamics of the impurity beyond the weak coupling assumptions of linear response theory. We show that the observed oscillation frequencies of the impurity–bath system can be mapped onto different physical states, and explain their dependence on bath density and strength of the impurity–bath interaction. In different limits, we see that the behaviour ranges from a tightly bound pair for strong interactions to polaron-like behaviour at weak interactions for a fermionic bath. The latter case is characterized by an interesting internal dynamics corresponding to the scattering between a bound pair and an impurity particle propagating through the fermionic bath. We also compare these results with the case of a bosonic bath to better define the role of the Fermi sea. Generally, we find that the physics for a boson bath can be qualitatively and even quantitatively similar to the fermionic case, for both the tightly-bound-pair and the polaron regime, provided the boson–boson repulsion is larger than the attractive interaction between the bath and the impurity.

This setup and characterization of the dynamics should be readily realizable with cold atoms in optical lattices, and we expect our zero-temperature results to hold also at finite temperature, provided it is lower than the energy scale given by the oscillation frequency.

This paper is organized as follows. We first introduce the system and describe the method used in section 1. There we also discuss the effects of combining a lattice potential with a trap in the case of an impurity that does not interact with the bath. In section 2, we present numerical results for the impurity dynamics and explain them both in the regimes of strong and weak interactions through a comparison with analytical methods. We discuss especially the frequency spectrum of oscillations, and identify different physical regimes of impurity behaviour. In section 3, we compare with the case of a bosonic reservoir, and identify similarities and differences to the case of the fermionic bath dependent on the boson–boson repulsion. In section 4, we discuss our findings and establish a connection to earlier impurity and polaron studies. Finally, the appendix contains details of several analytical results we have derived.

1. The fermionic system

1.1. The basic model and method

We consider a setup that is composed of an optical lattice, loaded with a number-imbalanced mixture of two hyperfine species of fermionic atoms, hereafter labelled \uparrow and \downarrow , which are confined to move along one dimension. Our interest lies in the case of extreme imbalance, namely $N_{\downarrow} = 1$ and $N_{\uparrow} \in \{1, \dots, L\}$, where L is the lattice size and $N_{\uparrow/\downarrow}$ is the total number of atoms for each species. In addition to the optical lattice, the \downarrow atomic impurity experiences a parabolic confining potential. For atoms in the lowest Bloch band, the system can be described by the Hubbard Hamiltonian ($\hbar \equiv 1$)

$$H = -J \sum_{i\sigma} c_{i\sigma}^{\dagger} c_{i+1\sigma} + \text{h.c.} + U \sum_i n_{i\uparrow} n_{i\downarrow} + V \sum_i n_{i\downarrow} \left(i - \frac{L-1}{2} \right)^2, \quad (1)$$

where J represents the hopping amplitude between neighbouring sites, $U < 0$ is the on-site (attractive) interaction energy and V characterizes the strength of the parabolic confining potential for the impurity. Throughout the paper we set $\hbar = 1$, and we choose as the length scale the lattice period a . Therefore, all energies are given in frequency units and all momenta are given in units of $1/a$.

To obtain the ground state of this Hamiltonian and simulate the full many-body dynamics after the impurity has received a kick with a defined quasi-momentum, we use a code based on the TEBD algorithm, more details of which can be found in e.g. [46–49]. In our simulations, we have considered a lattice size of $L = 200$ sites ($L = 400$ in one case), $N_{\downarrow} = 1$, $N_{\uparrow} = [1, 10, 20, \dots, 180, 190, 200]$ and $|U|/J = 0, 0.5, 1, 3, 5, 10, 20$ with particular emphasis on the case $|U|/J = 10$. At $t = 0^+$, a quasi-momentum k ($k = 0.1\pi$ unless otherwise stated) is imparted to the \downarrow impurity.

1.2. The non-interacting impurity

To provide a better description later on of the effects on the motion of an impurity that are induced by interactions with the bath, we first single out the dynamical effects induced by the concomitant presence of the harmonic trapping and the 1D lattice at $U = 0$. That is, we consider a single particle in a potential formed by combining a lattice and a harmonic potential. As shown in [50], if the particle is initially in the ground state of the combined potential and then the harmonic trap is displaced by an amount δ , the expectation value of the particle position is

$$\langle x \rangle = \delta \exp \left[- \left(\frac{\delta}{a_{\text{ho}}} \right)^2 \sin^2 (V/8t) \right] \cos \left[V \left(\sqrt{\frac{2}{Vm_{\text{eff}}}} - \frac{1}{4} \right) t - \frac{\delta^2}{2a_{\text{ho}}^2} \sin \left(\frac{Vt}{4} \right) + \frac{\pi}{2} \right], \quad (2)$$

where V is the strength of the trapping potential and m_{eff} is the effective mass of the particle in the lattice, which for our choice of units ($a = 1$) is $m_{\text{eff}} = 0.5J^{-1}$. The harmonic oscillator length is defined via the trapping frequency ω and the mass of the particle as $a_{\text{ho}} = 1/\sqrt{m_{\text{eff}}\omega}$, and on the other hand, the strength of the harmonic oscillator potential $V = m_{\text{eff}}\omega^2/2$: thus $a_{\text{ho}} = (2m_{\text{eff}}V)^{-1/4}$ and with $m_{\text{eff}} = 0.5J^{-1}$ we then should have $a_{\text{ho}} = (V/J)^{-1/4}$.

Our initial conditions involving a finite quasi-momentum kick differ from those in [50], where the harmonic trap is initially displaced by an amount δ . To account for this difference, we need to introduce a $\pi/2$ phase in the cosine term of equation (2), and also compute the value of δ corresponding to our initial momentum kick. We can do this by matching the energy of the initial state in each case. The energy for the state at $t \rightarrow 0^+$ is given by the lowest eigenenergy of the combined harmonic trap and lattice system (equation (14) of [50]), with the addition of the kinetic energy given by the kick of a quasi-momentum k . If, by a semiclassical argument, we assume that this energy must be converted to potential energy (removing the zero-point energy from both the terms), then we have

$$V \left(\delta^2 + \frac{1}{16} + \frac{\sqrt{V/J}}{256} \right) = (1 - \cos k)/m_{\text{eff}}. \quad (3)$$

The left-hand side of equation (3) represents the small V expansion of the potential energy of a particle in a 1D lattice in the presence of harmonic confinement when displaced by δ from the minimum of the potential, while the right-hand side is its kinetic energy. We can thus deduce an approximate expression for δ :

$$\delta = \left[\frac{1 - \cos k}{Vm_{\text{eff}}} - \frac{1}{16} - \frac{\sqrt{V/J}}{256} \right]^{1/2}. \quad (4)$$

Combining equations (2) and (4), we obtain the relation between the centre of mass (COM) oscillation frequency ω_{COM} and the theoretical value of the mass of the different particles

$$\omega_{\text{COM}} = V \left[\left(\sqrt{\frac{2}{m_{\text{eff}}V}} - \frac{1}{4} \right) - \frac{\sqrt{V/J}}{4} \left(\frac{1 - \cos k}{m_{\text{eff}}V} - \frac{1}{16} - \frac{\sqrt{V/J}}{256} \right) \right]. \quad (5)$$

As a benchmark, we have compared the frequency given by equation (5) with the value obtained from the numerical simulations for a free particle ($m_{\text{eff}} = 0.5$), and we found good agreement between analytical and numerical values.

2. Dynamics of an impurity in a fermionic bath

In the following, we characterize the different physical states which the impurity may form inside the bath. The key observable in our analysis is the oscillation of the time-dependent *doublon density*, defined as $\langle n_{i \uparrow} n_{i \downarrow} \rangle(t)$, after a kick with quasi-momentum $k = 0.1\pi$ has been imparted to the impurity at $t = 0^+$. We find that this is a more useful quantity than the impurity density $\langle n_{i \downarrow} \rangle(t)$, as it provides more direct information corresponding to the bath dynamics and pairing with the impurity.

Examples of the oscillatory motion of the doublon density are shown in figures 1 and 2 in the regime of strong ($|U|/J = 10$) and weak ($|U|/J = 1$) attraction, respectively. In the strongly attractive case, we see the oscillation frequency shifting as a function of the bath filling, increasing only slightly while the bath density is below half-filling, but jumping to much larger values above, from where it decreases again as the density approaches integer filling. Conversely, in the case of weak attraction the oscillation frequency only decreases slightly for low and high densities, and is roughly the same for all intermediate densities.

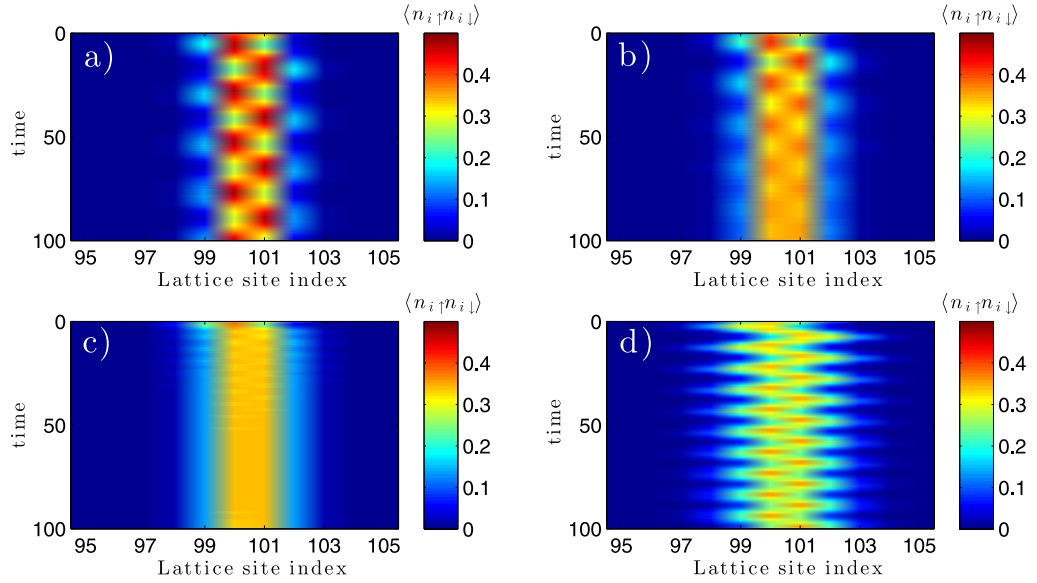


Figure 1. Time dependence of the local doublon density $\langle n_{i\uparrow}n_{i\downarrow} \rangle$ for $|U|/J = 10$ and $N_{\uparrow} = 20$ (a), 60 (b), 140 (c) and 180 (d). The horizontal axis: site index i ; the vertical axis: time (in units of J^{-1}). In the simulations, we first calculate the ground state of the lattice (number of lattice sites $L = 200$) loaded with one impurity ($N_{\downarrow} = 1$), in the presence of a bath of spin-up particles (different simulations were performed with varying numbers of up particles $N_{\uparrow} = [1, 10, 20, \dots, 180, 190, 200]$), whose description is provided by the Hubbard Hamiltonian. In addition to the attractive interaction between spin-up and spin-down particles, characterized by the parameter U , the impurity is confined by a parabolic potential of the form $V i^2$, with i the site index, and $V/J = 0.1$. At $t = 0^+$, the down particle is kicked with quasi-momentum $k = 0.1\pi$. As is described in the text, it is possible to see that, as a function of N_{\uparrow} , the dynamics exhibits different regimes, characterized by a transition from doublon oscillations to a regime where the internal dynamics of the polaron dominates, and eventually to free-particle oscillations. All simulations are performed with a TEBD code, with the following numerical parameters: lattice size $L = 200$, unless otherwise stated; Schmidt number $\chi = 80$; initial imaginary timestep (ground-state calculation) $\delta t_i = 0.1 J^{-1}$; timestep (real-time evolution) $\delta t = 0.02 J^{-1}$ (throughout the paper $\hbar = 1$, and the length scale is set equal to the lattice spacing a , see the text). After testing with larger values of the Schmidt number, we have used the value $\chi = 80$, which provides accurate results both for the ground state and the time evolution. The reason for the effectiveness of this rather small value of χ lies in the reduced size of the Hilbert space for a strongly imbalanced gas.

The observable that encapsulates all these behaviours is the doublon centre of mass ($\mathcal{X}_{\uparrow\downarrow}$), defined as

$$\mathcal{X}_{\uparrow\downarrow}(t) = \frac{\sum_i (i - \frac{L-1}{2}) \langle n_{i\uparrow}n_{i\downarrow} \rangle(t)}{\sum_i \langle n_{i\uparrow}n_{i\downarrow} \rangle(t)},$$

which is extracted from the full density and is shown in figures 3 and 4.

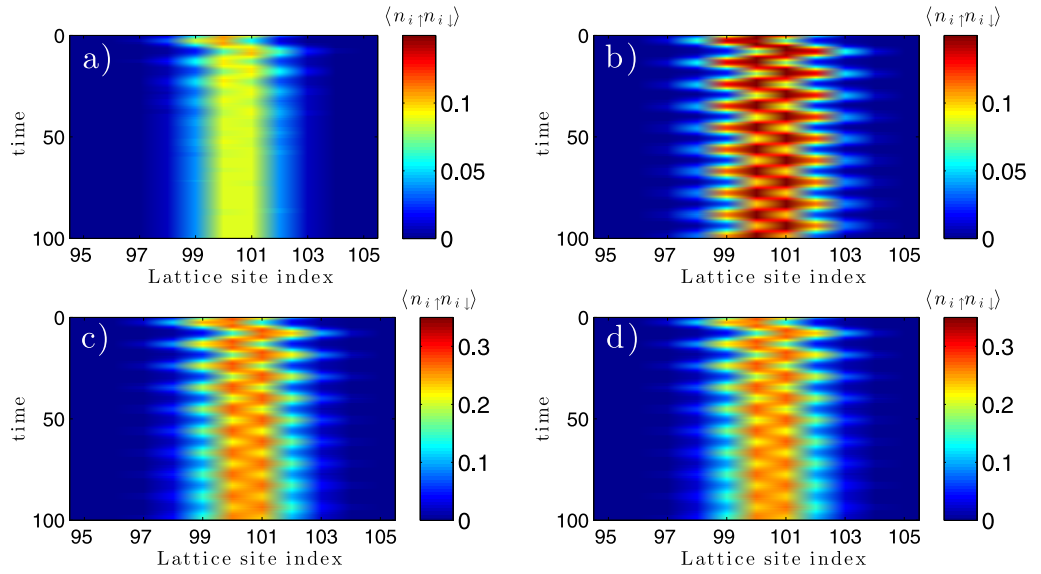


Figure 2. Time dependence of the local doublon density $\langle n_{i\uparrow}n_{i\downarrow} \rangle$ for $|U|/J = 1$ and $N_{\uparrow} = 20$ (a), 60 (b), 140 (c) and 180 (d). For $|U|/J = 1$, the time evolution of $\langle n_{i\uparrow}n_{i\downarrow} \rangle$ is characterized by single-particle oscillations decreasingly damped for increasing bath particle population. For $N_{\uparrow} = 20$, small-amplitude oscillations (not visible here, see figure 6) appear; these oscillations are associated with the pair-breaking mechanism as we will discuss in section 2.3. All simulation parameters (except U) are the same as in figure 1.

As is explained in detail in the following sections for the different interaction and bath density regimes, we gain insight into the physics of the system by analysing the Fourier transform of $\mathcal{X}_{\uparrow\downarrow}(t)$, $\mathcal{X}_{\uparrow\downarrow}(\omega)$, which is shown in figures 5 and 6 for strong and weak attraction. For strong attraction, $\mathcal{X}_{\uparrow\downarrow}(\omega)$ shows that the oscillation of a tightly bound on-site pair dominates the dynamics at low density, while a polaron-like state is present but weak (low- and high-frequency peaks in figure 5(a), respectively). The relative weights of the polaronic and bound-pair peaks reverse as the density of bath atoms increases above 0.5, with the polaron component becoming predominant and the bound-pair peak almost vanishing (high- and low-frequency peaks in figure 5(b), respectively; note, e.g., how for $N_{\uparrow} = 140$ the bound-pair peak has become essentially just a broad shoulder).

In order to understand the physics of the bound pair for strong interactions between the impurity and the bath atoms, we make use of the so-called string hypothesis from the Bethe-ansatz solution of the Hubbard model (cf section A.1 of the appendix). Using this, we see that a tightly bound on-site pair dominates at low bath fillings, and can be understood in a two-body picture, where we can compute formulae for the pair oscillation frequency, as shown in figure 7. On the other hand, the polaron-like state dominating at higher densities can be explained by the scattering of bath particles from the Fermi surface to the edge of the Brillouin zone mediated by the oscillating impurity. We find that the frequency of the resultant peak in $\mathcal{X}_{\uparrow\downarrow}(\omega)$ is insensitive to the value of both the interaction strength U and the initial momentum kick k . We also examine the way the impurity modifies the density of the bath around its position, and explain why the

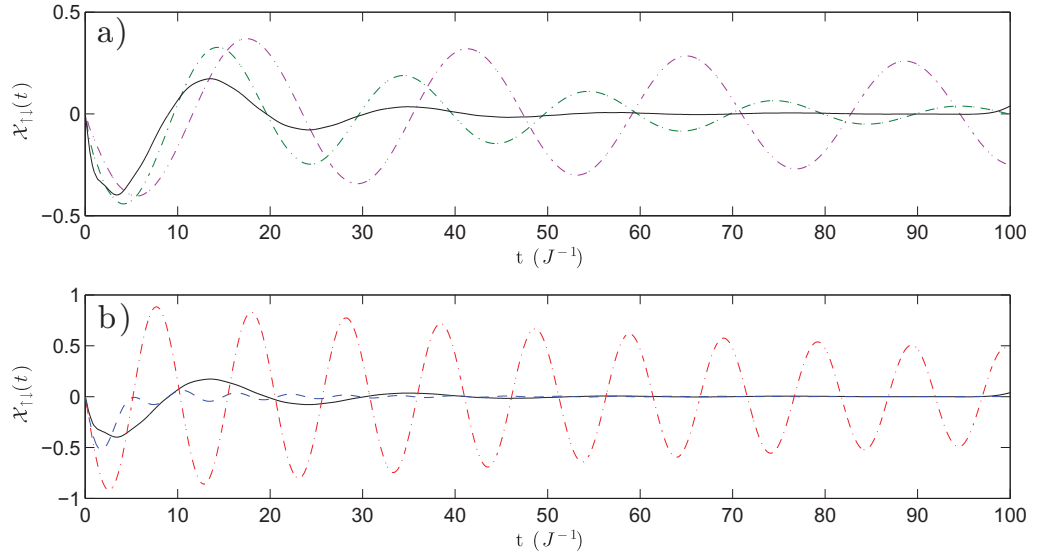


Figure 3. The doublet centre of mass $\mathcal{X}_{\uparrow\downarrow}(t)$ for $|U|/J = 10$ and (a) $N_{\uparrow} = 20$ (purple curve), 60 (green dash-dotted curve), 100 (black continuous curve); and (b) $N_{\uparrow} = 100$ (black continuous curve), 140 (blue dashed curve), 160 (red curve). In panel (a), it is possible to see how the centre-of-mass oscillations associated with the doublet dynamics are increasingly damped when the bath population increases towards half-filling. Above half-filling, the oscillations associated with the polaron internal dynamics (described in section 2.2) start to appear, reaching the free-particle oscillation frequency for $N_{\uparrow} \rightarrow L$. The deviation of $\mathcal{X}_{\uparrow\downarrow}$ for $t \rightarrow 100J^{-1}$ is a finite-size effect. It corresponds to the time for which excitations in the bath are reflected back from the system boundaries to the centre of the trap, affecting thus the doublet dynamics. All simulation parameters are the same as figure 1.

peak position stays independent of U despite this local distortion. Section 2.2 describes this in detail, including the change in the polaron oscillation frequency with density.

In contrast, in the case of weak interaction, a polaron component to the oscillation is significant only for densities at or below 0.2 (low-frequency peak in figure 6(a), while the dominant component of $\mathcal{X}_{\uparrow\downarrow}(\omega)$ stems from the motion of a free particle (low- and high-frequency peaks in figures 6(a) and (b), respectively). In this regime, the polaronic component corresponds to the resonant scattering between a bound pair and an impurity particle propagating through the background particle bath. This will be described in section 2.3.

2.1. Strong interactions: the low-frequency peak

In a 1D Hubbard model with strong interactions, Bethe-ansatz techniques provide two sets of solutions, which together cover all possible eigenstates of the system—provided that we assume the so-called string hypothesis to be correct [30]. In each of these two sets of solutions, A and B, the total energy E and quasi-momentum P of a many-body state can be expressed in terms of Bethe-ansatz quantum numbers $\{k_i\}$ and Λ .

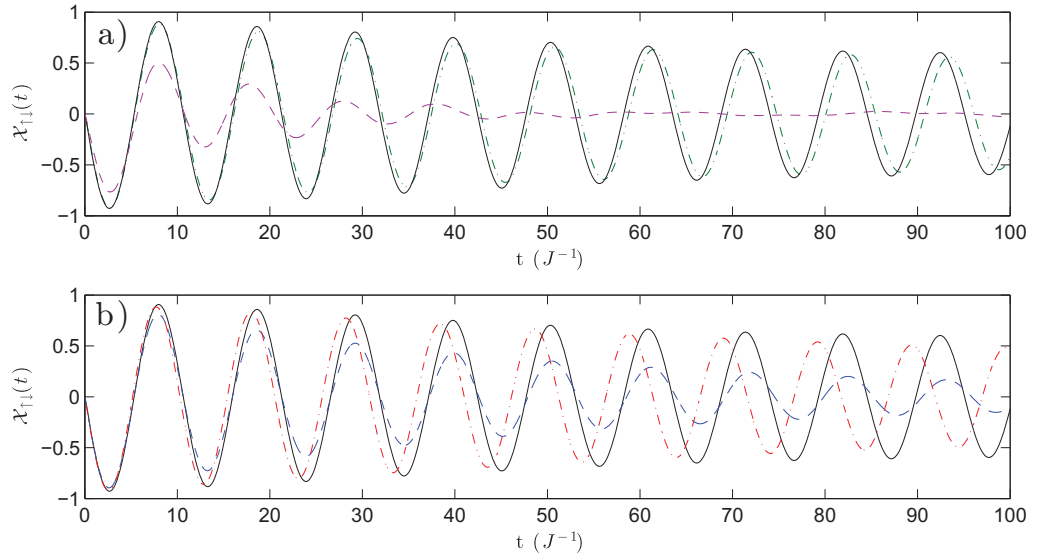


Figure 4. The centre of mass $\mathcal{X}_{\uparrow\downarrow}(t)$ for $|U|/J = 1$ and (a) $N_{\uparrow} = 20$ (purple dashed curve), 60 (green dash-dotted curve), 100 (black continuous curve) and (b) $N_{\uparrow} = 100$ (black continuous curve), 140 (blue dashed curve), 160 (red curve). For $|U|/J = 1$, the oscillations are dominated by the single-particle oscillation frequency $\omega/J \simeq 0.62$ and increasingly damped for decreasing bath population. All simulation parameters are the same as in figure 2.

For the solutions of type A

$$P = \sum_{j=1}^N k_j, \quad E = -2J \sum_{j=1}^N \cos(k_j) + \text{const.} \quad (6)$$

and for the solutions of type B,

$$P = \sum_{j=1}^{N-1} k_j + 2q, \quad E = -2J \sum_{j=1}^{N-1} \cos(k_j) - 4J \cosh \xi \cos(q) + \text{const.}, \quad (7)$$

where ξ is defined by

$$\cosh \xi = \sqrt{1 + \frac{U^2}{16J^2 \cos^2(q)}} \quad (8)$$

and q is the real part of the quantum numbers associated with the $k - \Lambda$ string (see section A.1 of the appendix). In the strong coupling limit, it is possible to show that

$$-4J \cosh \xi \cos q \rightarrow U - 4J^2/|U| - 4J^2/|U| \cos(\kappa) + O\left(\frac{1}{U^2}\right), \quad (9)$$

where $\kappa = 2q$ is the total quasi-momentum of the pair.

The eigenstates of type A correspond to the effectively free motion of both the bath particles and the impurity, while solutions of type B correspond to a bound state of the impurity with one bath atom (with the remaining $N_{\uparrow} - 1$ bath atoms again moving freely) (see section A.1 of the appendix). For an attractive interaction, the B-type solutions are always energetically

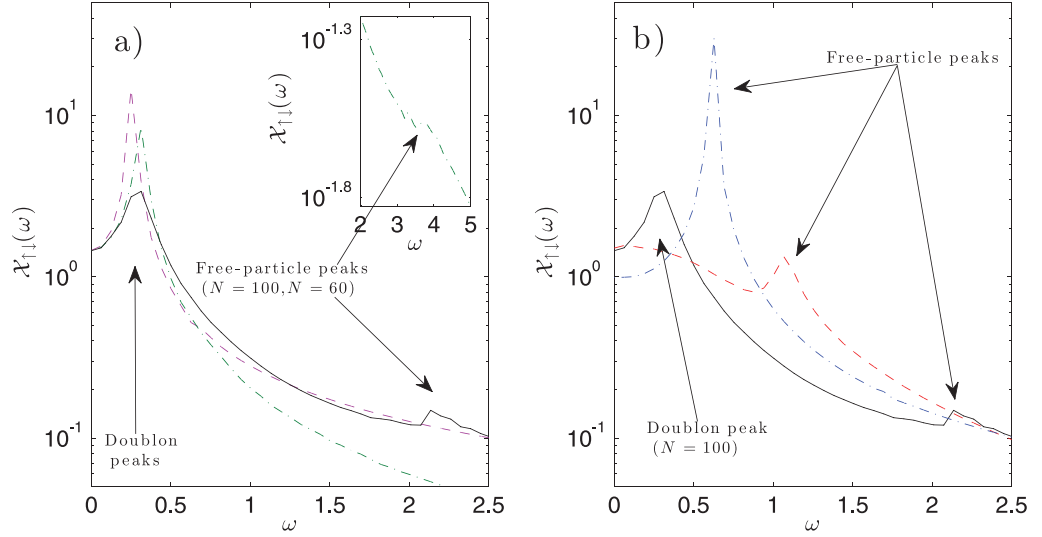


Figure 5. The doublet centre of mass $\mathcal{X}_{\uparrow\downarrow}(\omega)$, $|U|/J = 10$. The Fourier analysis allows a quantitative estimation of the oscillation frequencies for different values of N_{\uparrow} , complementing the description given in figure 3. (a) $N_{\uparrow} = 20, 60, 100$ (purple dashed, green dash-dotted and black continuous curves). For $N_{\uparrow} = 20$ only the doublon peak for $\omega/J \simeq 0.5$ is present, while for $N_{\uparrow} = 100$ the polaron internal dynamics peak appears, for $\omega/J \simeq 2.1$, respectively, and for $N_{\uparrow} = 60$ the precursor of the polaron peak starts to appear around $\omega/J \simeq 3.8$. The inset shows additional data for higher values of ω . (b) $N_{\uparrow} = 100, 140, 180$ (black continuous, blue dashed, and red dash-dotted curves). The polaron internal dynamics peak shifts to the left for increasing interaction ($\omega/J \simeq 2.1, 1.1, 0.8$ for $N_{\uparrow} = 100, 140, 180$), while the doublon peak is increasingly damped. All simulation parameters are the same as in figure 1.

favourable, and for $|U|/J > 2$ there is no overlap between the bands associated with type-A and type-B solutions.

Thus focusing on the B-type manifold of eigenstates, we can describe the observed behaviour of the low-frequency peak in $\mathcal{X}_{\uparrow\downarrow}(\omega)$ at large $|U|$ (cf figure 5) by deriving the explicit expression for the many-body energy E in equation (7) as a function of the doublon quasi-momentum κ (see section A.1 of the appendix) to be

$$E_{\kappa} = -\sqrt{U^2 + 16J^2 \cos^2(\kappa/2)}, \quad (10)$$

where the dependence of the energy on the other $N_{\uparrow} - 1$ quasi-momentum quantum numbers $\{k_i\}$ has not been taken into account, being irrelevant in the dynamics considered here. From this, the effective mass of the tightly bound pair can be extracted to be

$$m_{\text{doublon}} = \left[\left(\frac{\partial^2 E}{\partial \kappa^2} \right) \right]_{\kappa \rightarrow 0}^{-1} = \frac{1}{J} \sqrt{1 + \frac{U^2}{16J^2}} \xrightarrow{|U|/J \gg 1} \frac{|U|}{4J^2}, \quad (11)$$

which, in the limit $|U|/J \ll 1$, coincides with the expression that would be obtained from second-order perturbation theory.

It is interesting to note that our Bethe-ansatz solution delivers the same result for the quasi-momentum dependence of the doublon contribution to the energy as the simple solution to

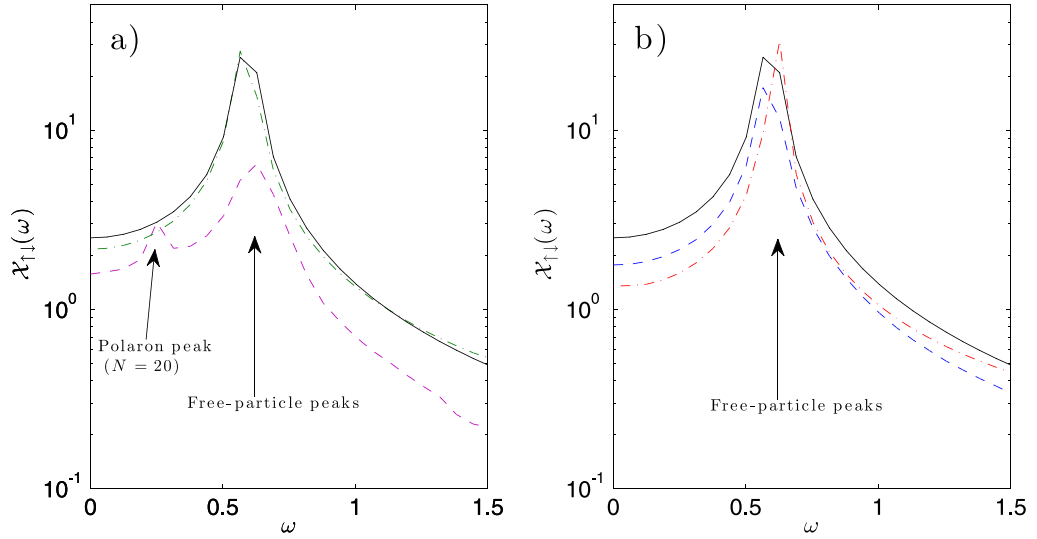


Figure 6. $\mathcal{X}_{\uparrow\downarrow}(\omega)$, $|U|/J = 1$. (a) $N_{\uparrow} = 20, 60, 100$ (purple dashed, green dash-dotted and black continuous curves) and (b) $N_{\uparrow} = 100, 140, 180$ (black continuous, blue dashed and red dash-dotted curves). For $N_{\uparrow} = 20$ both the polaron and the free-particle peaks are present ($\omega/J \simeq 0.4, 0.8$, respectively, while for larger values of N_{\uparrow} , only the free-particle peak is present. All simulation parameters are the same as in figure 2.

the problem of two distinguishable bound particles on a lattice [51, 52]. In figure 7, we show the comparison between the numerical value of the doublon peak oscillation frequency (low-frequency peak in the strong-interaction regime), and the theoretical value obtained using our value for the doublon mass (11) in conjunction with equation (5). The excellent agreement seen shows that the doublon dynamics is well captured by our Bethe-ansatz-based model.

2.2. Strong interactions: the high-frequency peak

In the case of strong attraction (large $|U|$) treated in this section, the oscillations of the doublon density also show another, high-frequency component in $\mathcal{X}_{\uparrow\downarrow}(t)$, which is weak for low bath densities, but which becomes significant above half-filling (see figure 5). Here, we argue that this feature can be understood in terms of an effective scattering of bath particles from the Fermi surface off the oscillating impurity towards the edge of the Brillouin zone. We will show that the position of this high-frequency peak in $\mathcal{X}_{\uparrow\downarrow}(\omega)$ depends primarily on the filling fraction in the bath and the associated value of k_F , and is essentially independent of the kick strength and insensitive to U .

2.2.1. Description of the dynamics in terms of particle–hole excitations of the bath. The high-frequency peak in the strongly interacting limit can be understood in terms of scattering between two bath particles mediated by the presence of the impurity, together with the dynamics of the impurity itself. Within the framework of a two-band model (see figure 8), the effective scattering between bath particles is explained in terms of an exchange process, involving the transfer of

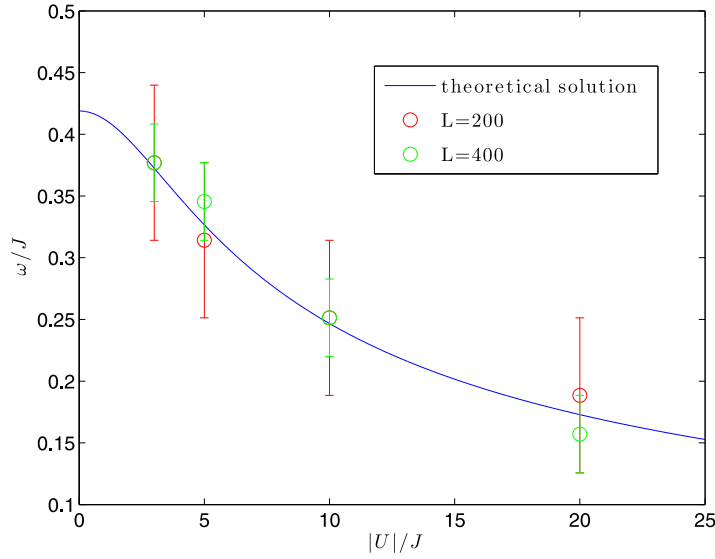


Figure 7. Comparison between the numerical value of the low-frequency peak oscillation frequency for the large interaction case (as extracted from $\mathcal{X}_{\uparrow\downarrow}(\omega)$), and the theoretical value for $|U|/J > 1$, given by equations (10) and (11)). This comparison allows us to establish that the low-frequency oscillations of $\mathcal{X}_{\uparrow\downarrow}$ can be described in terms of oscillations of a particle (composed of one spin-up and one spin-down particle) in a parabolic confining potential. All simulation parameters are the same as in figure 1, except for the interaction strength and the lattice size. Here $|U|/J = 3, 5, 10, 20$ and $L = 200$ or 400 . The error bars account for the finite resolution of the Fourier transform. Larger lattices allow for longer simulation times before the reflection from the edges starts playing a role in the doublon dynamics, thus allowing higher resolutions in the frequency domain. It is worth noting that the full Bethe-ansatz formula works even for moderately weak interaction. The characteristic size of the composite particle is given by ξ^{-1} (see figure A.1), corresponding to a value of $\simeq 2.3$ for $|U|/J = 3$.

the up particle from the tightly bound pair to the \uparrow -particle band above the Fermi level, and the concomitant transfer of a particle from the Fermi surface to the tightly bound pair (see figure 8).

The total energy necessary for this process, which the initial kick must supply now, involving both the scattering process and the impurity dynamics, is given by

$$\Delta E = \omega_{hi} + 2J \left[(1 - \cos k_p) - (1 - \cos k_{F\uparrow}) \right], \quad (12)$$

where ω_{hi} is the oscillation energy associated with the dynamics of the impurity in a completely full bath-particle band. The frequency ω_{hi} thus corresponds to the oscillation frequency of a free particle in the lattice, in the presence of the parabolic confining potential V , and its value can be calculated from equation (5).

The term $2J(1 - \cos k_p)$ corresponds to the transfer of an ' \uparrow ' particle from the tightly bound pair to a free state of the bath above the Fermi level, as sketched in figure 8. The term $(1 - \cos k_{F\uparrow})$ then is related to the transfer of an \uparrow -particle from the Fermi surface of the bath to the bound state of the $\uparrow\downarrow$ - pair.

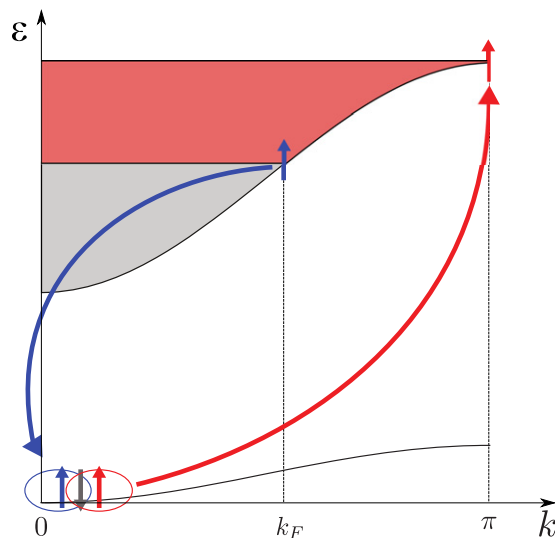


Figure 8. Two-band process leading to the scattering of a bath particle from k_F to π . The specific pair-mediated process depicted here ($k_p = \pi$) represents the process associated with the maximum energy transfer from the pair to the bath. The promotion of an \uparrow particle from the pair to the bath is allowed for $k_F < k < \pi$, while for $0 < k < k_F$ the process is forbidden due to Pauli blocking.

In figure 9, we show how the position of the high-frequency peak depends on the bath density—provided by numerics—and that it is in reasonable agreement with the expression given by equation (12) when $k_p = \pi$, corresponding to the largest possible energy associated with the transfer of an \uparrow -particle from the pair to the bath (see figure 8). We further find the peak position to be insensitive to changes in U and kick strength k .

The offset between numerical results and equation (12) is then related to the non-uniform spatial distribution of k_F for the bath particles. This non-uniformity, in turn, is due to the perturbing effect of the impurity, which can be approximated as Friedel oscillations in the bath as we will show below. As the spatial extent of Friedel oscillations does not depend on $|U|$, the spatial distribution of k_F and consequently ΔE are independent of the strength of the interaction. These findings go some way towards explaining why even the local density disturbance of the bath by the impurity is congruent with the observed U independence of the high-frequency peak.

2.2.2. Bath-particle distribution in the presence of an impurity. With attractive interactions and an impurity that is localized by the tight parabolic confinement potential, the density of bath particles is modified locally in the centre of the system. Let us denote the size of this modified region of the bath by ζ . We make a first estimate of the value of ξ by considering the limiting case $U \rightarrow -\infty$, with the impurity being located on a single site, i . In this case, due to the limit of infinite attraction, the site i will act as a hard-wall boundary condition [53, 54], and the density profile of the bath particles around the impurity will undergo Friedel oscillations [55] (see figure 10), as was recently pointed out in [28] for repulsive interaction and in the absence

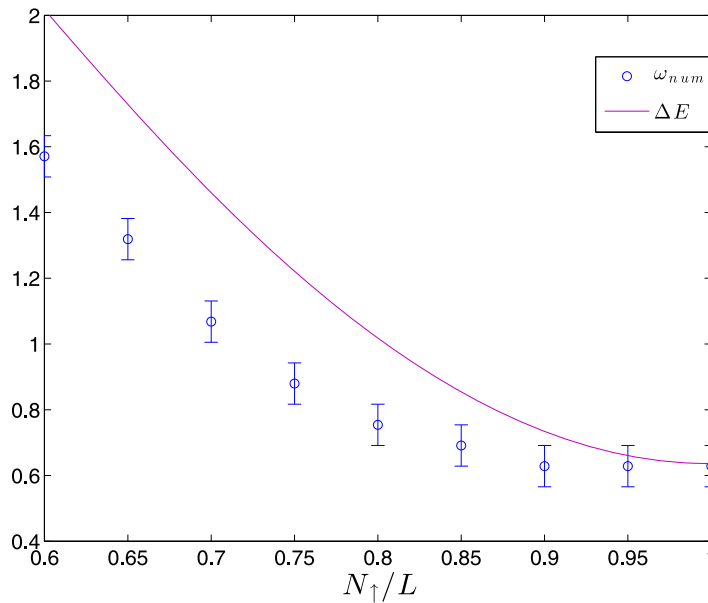


Figure 9. Plot of the high-frequency peak as a function of the bath filling, compared to the value of ΔE obtained from equation (12), for $k_p = \pi$. The position of the peaks in the numerical results does not show any dependence on k and U : the value of ω_{num} coincides for $k = 0.05\pi$, 0.1π , 0.25π and $|U| = 10$, and $k = 0.1\pi$ and $|U| = 5$.

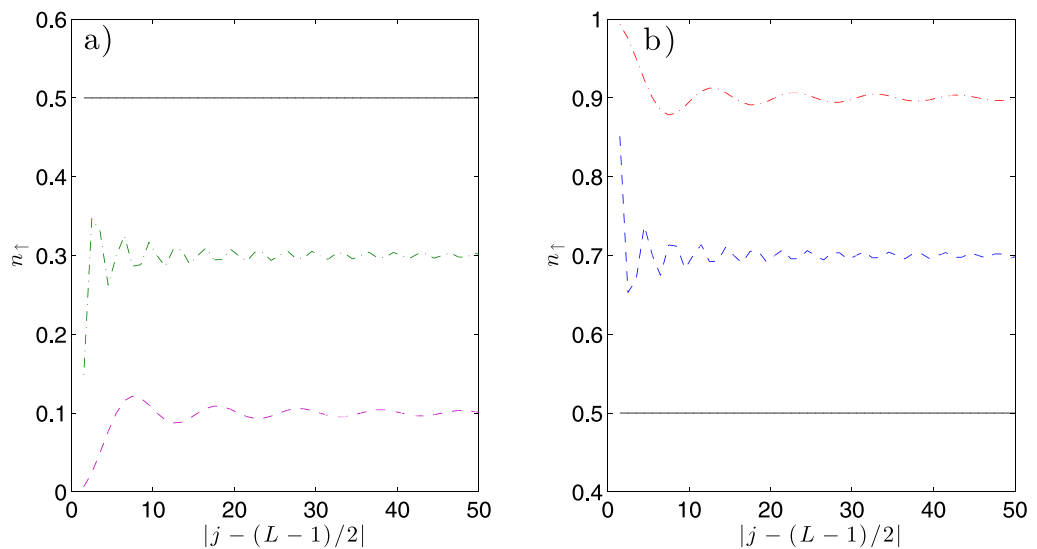


Figure 10. Friedel oscillations (see equation (13)) induced by the presence of a hard-wall boundary condition at $j = (L - 1)/2$ for (a) 20 (purple dashed curve), 60 (green dash-dotted curve), 100 (black continuous curve) and (b) 100 (black continuous curve), 140 (blue dashed curve), 180 (red dash-dotted curve) bath particles, respectively (see equation (13)).

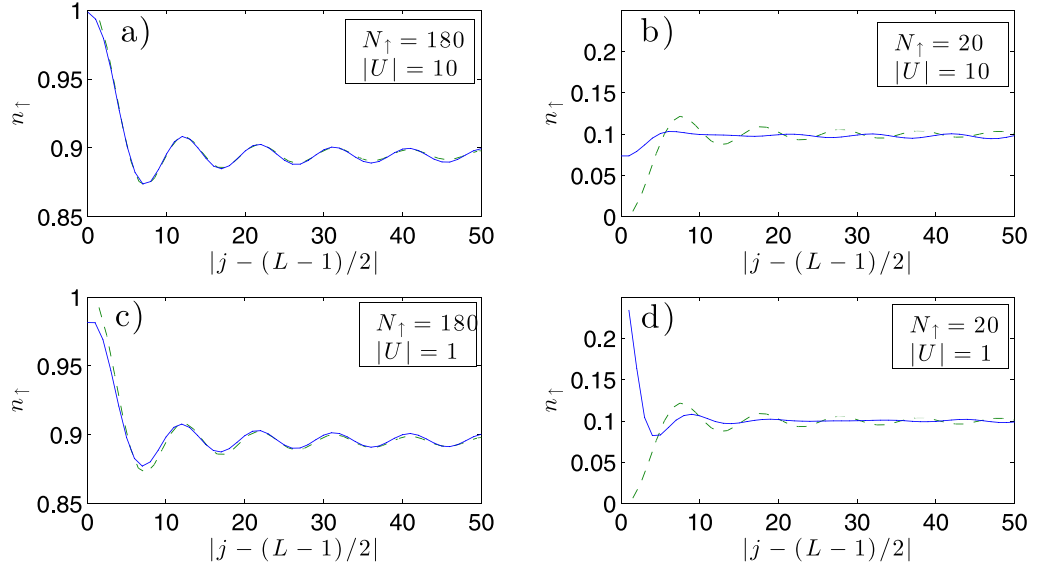


Figure 11. Comparison between the numerical estimate of the ground-state spatial oscillations induced in the bath by (a), (c), (d) a single down impurity or (b) a doublon (blue continuous curves), with the Friedel oscillations induced by hard-wall boundary conditions (green dash-dotted curves), with (a) $N_{\uparrow} = 180$, $|U|/J = 10$, (b) $N_{\uparrow} = 20$, $|U|/J = 10$, (c) $N_{\uparrow} = 180$, $|U|/J = 1$ and (d) $N_{\uparrow} = 20$, $|U|/J = 1$. In the high-density limit, there is good agreement between the numerical calculations and the approximate model, while in the low-density limit, the numerical results suggest that the role of the impurity cannot be described in terms of an impurity-induced Hartree potential. This hypothesis is confirmed by the exact diagonalization of an Hamiltonian describing a spin-polarized gas in the presence of a localized potential mimicking the potential induced by the impurity. In this case the results are compatible with the results implied by equation (13). All simulation parameters are the same as in figures 1 and 2.

of the lattice, according to the following formula:

$$\rho_{\uparrow}(j) = \frac{N_{\uparrow}}{L} - \frac{1}{2\pi} \frac{\sin[2k_{F\uparrow}(j-i)]}{|j-i|}. \quad (13)$$

We note that in a 1D system the period of these oscillations is always independent of the strength of the interactions between the bath particles and the bath impurity interactions, and is *always* $(2k_{F\uparrow})^{-1}$ for a fermionic bath, and $(2\pi\rho_0)^{-1}$ for a bosonic one—all that changes with the interaction is the amplitude of the Friedel oscillations.

In figure 11, we show how approximating either the on-site bound pair (in the case of strong attraction) or the single particle (for weak attraction) as a boundary condition located at the minimum of the parabolic potential works well to describe the density modulation induced in the bath when N_{\uparrow} is large, while it fails in the case of a more dilute system. As we have been focusing on just this regime of intermediate and high filling in this part, this approximation should be very reasonable.

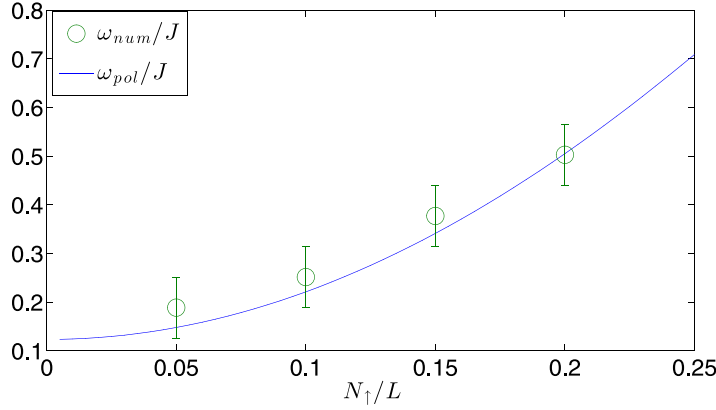


Figure 12. Comparison between the numerical value of the low-frequency peak at $|U|/J = 1$ and the ω_{pol} corresponding to the resonant frequency of the bound-doublon to scattering-states transition. This peak can be seen in the $N_{\uparrow} = 20$ plot (a small peak around $\omega \simeq 0.2$ in figure 6). Above $N_{\uparrow}/L \simeq 0.2$, it merges with the free-particle peak, and eventually disappears. In this picture, the spin-up bath particles are resonantly bound to the spin-down impurity, analogous to the case of static polarons. All simulation parameters are like those in figure 2. The error bars account for the finite resolution of the Fourier transform.

2.3. Weak interactions

As anticipated, for interactions $|U| \leq 1$, the peak in $\mathcal{X}_{\uparrow\downarrow}(\omega)$ associated with the oscillation of a tightly bound on-site pair is not present. Nevertheless, we observe two distinct modes in the doublon-density centre-of-mass oscillations $\mathcal{X}_{\uparrow\downarrow}(t)$ in the weakly interacting regime as well. One of them appears due to the free oscillatory motion of a non-interacting particle as derived in section 1.2. Another peak, at lower frequencies, appears as well (see figures 6 and 12).

The underlying physics of this low-frequency peak derives from a resonant transition between a bound pair and scattering states, specifically the spin-down impurity at zero quasi-momentum and a spin-up bath particle at the Fermi quasi-momentum $k_{F\uparrow}$. The frequency of this peak can thus be obtained considering the difference between the energy of the (weakly bound) pair and the energy of the scattering state

$$\omega_{pol} = E_{\uparrow} + E_{\downarrow} - E_{\uparrow\downarrow} = -2J [1 + \cos(k_{F\uparrow})] + \sqrt{U^2 + 16J^2}. \quad (14)$$

Figure 12 shows excellent agreement between this model and the numerical results of the TEBD calculations, within the error bars set by the finite resolution of the Fourier transform.

Further, the existence of the two peaks in $\mathcal{X}_{\uparrow\downarrow}(\omega)$ can be related to the known structure of the polaron ground state: in the polaron ansatz [12] of the type

$$|\Psi\rangle = \sqrt{Z} c_{0\downarrow}^{\dagger} |FS\rangle_{\uparrow} |0\rangle_{\downarrow} + \sum_{k > k_{F\uparrow}, q < k_{F\uparrow}} \phi_{k,q} c_{k\uparrow}^{\dagger} c_{q\uparrow} c_{q-k\downarrow}^{\dagger} |FS\rangle_{\uparrow} |0\rangle_{\downarrow}, \quad (15)$$

the first term describes the impurity at rest in the presence of the unperturbed Fermi sea of the bath (with the quasi-particle weight Z), and the second term a coherent superposition of states in which the motion of the impurity is correlated with a single particle-hole excitation of the Fermi sea (like the weakly bound state entering equation (14)).

We can hypothesize that the high-frequency ‘free particle’ peak in $\mathcal{X}_{\uparrow\downarrow}(\omega)$ corresponds to a second-order process involving the virtual breaking of a pair, while the low-frequency peak is caused by the breaking up of the correlated state between the impurity and a particle–hole excitation of the Fermi sea.

2.4. Damping

Along the lines of the above discussion on the particle–hole excitation process, it is possible to intuitively understand the oscillation damping. When approaching half-filling, both from the low- and the high-density limit, the oscillation damping is increased. This increase is associated with the increase of the particle–hole creation mechanism through the virtual breaking of a pair for increasing filling, and the concomitant energy transfer increase for decreasing filling. This mechanism of dissipation is confirmed by the observation in the numerical data of density perturbations in the bath particles, propagating at $2J$, consistent with the picture of the transfer of bath particles to the top of the band $k = \pi$.

3. The kicked impurity in a bosonic reservoir

Comparing the results obtained for a fermionic reservoir to those from a bosonic one enables us to state which features of the observed dynamics are universal and which are particular to the fermionic bath. Towards achieving this, we have performed TEBD simulations for a two-species Bose–Hubbard Hamiltonian,

$$H = -J \sum_{i\sigma} b_{i\sigma}^\dagger b_{i+1\sigma} + \text{h.c.} + U \sum_i n_{i\uparrow} n_{i\downarrow} + \frac{W}{2} \sum_i n_{i\uparrow} (n_{i\uparrow} - 1) + V \sum_i n_{i\downarrow} \left(i - \frac{L-1}{2} \right)^2, \quad (16)$$

where the trap parameter V , tunnelling J and the values of U and N_\uparrow are the same as described in section 1, as is the impurity preparation and the initial kick to the impurity (as in the fermionic case, we will set $J = 1$, $a = 1$). The two key differences are that now $b_{i\sigma}$, $b_{i\sigma}^\dagger$ are operators for soft core bosons, which interact repulsively on-site with energy W , if $\sigma = \uparrow$. Here, we have considered $W/J = 4, 10, 20$.

3.1. The weak interaction limit

Repeating the TEBD simulations for weak interactions between the impurity and a bosonic bath, we find that the two-peak structure discussed in section 2.3 persists for all the values of W we have simulated, as shown in figure 13. Moreover, the position of the polaron-dissociation peak (cf section 2.3) is still described remarkably well by the theory for the fermionic bath even for the lowest value of W , $W/J = 4$. These findings can be understood analytically by observing that, at low densities and reasonably large values of W , 1D lattice bosons map to spinless fermions with weak nearest-neighbour attractions. This mapping is achieved by describing the sector of low-energy, long-wavelength excitations of the \uparrow component of the Hamiltonian (16) as a Tomonaga–Luttinger liquid (TLL), whose properties are characterized by the so-called TLL parameters, K_b and v_b [56]. Expanding the \uparrow -sector in Hamiltonian (16) and the bath density

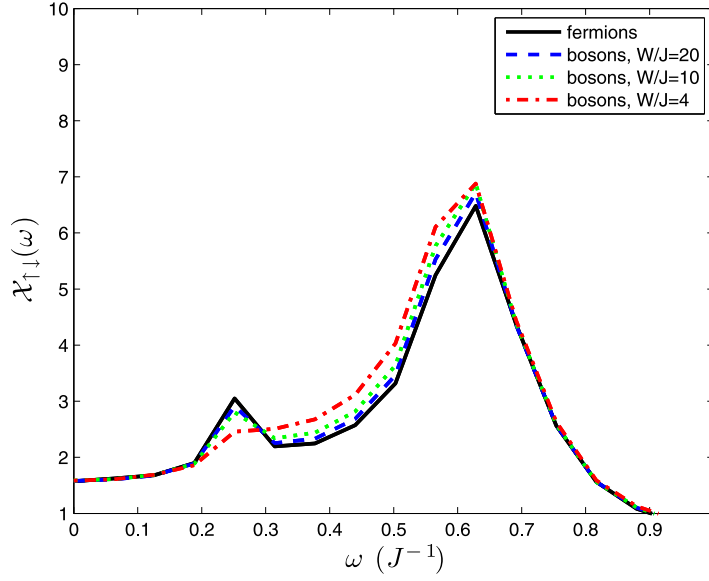


Figure 13. Comparison of $\mathcal{X}_{\uparrow\downarrow}(\omega)$ between fermions and bosons in the weak-attraction case, $|U|/J = 1$, $N_{\uparrow} = 20$. The position of the low-frequency peak for the fermionic bath, which stems from a break-up of correlated states between the impurity and particle-hole excitations in the bath (cf section 2.3), is very similar to that for the bosonic bath, at all values of W . See the text for details.

operator $n_{x\uparrow}$ in terms of the canonically conjugate TLL field operators $\phi_{\uparrow}(x)$ and $\theta_{\uparrow}(x)$, one obtains

$$\begin{aligned}
 H \approx & \frac{1}{2\pi} \int dx \left(u_b K_b (\partial_x \theta_{\uparrow}(x))^2 + \frac{u_b}{K_b} (\partial_x \phi_{\uparrow}(x))^2 \right) \\
 & + U \sum_i \left(\rho_0 - \frac{\partial_x \phi_{\uparrow}(x_i)}{\pi} \right) \left(\sum_{m=-\infty}^{\infty} e^{2im[\pi\rho_0 x_i - \phi_{\uparrow}(x)]} \right) n_{i\downarrow} \\
 & + J \sum_i b_{i\downarrow}^{\dagger} b_{i+1\downarrow} + \text{h.c.} + V \sum_i n_{i\downarrow} \left(i - \frac{L-1}{2} \right)^2, \quad (17)
 \end{aligned}$$

where expanding the impurity-bath coupling in this way presupposes that the impurity does not distort the bath density too much locally. In the limit of large W/J , the TLL parameters are known perturbatively, $K_b \approx 1 + \frac{4J}{\pi W} \sin \pi \rho_0$, $u_b = 2J \sin \pi \rho_0 \left(1 - \frac{4J}{W} \rho_0 \cos \pi \rho_0 \right)$.

Now, a bath of spinless lattice fermions with attractive nearest-neighbour interactions V_{nn} and Fermi quasi-momentum k_F coupled to an impurity with an on-site density-density interaction, can be mapped to a TLL in 1D in a manner identical to (17), where K_b is replaced by K_f and u_b by u_f [29]. These parameters are also known from perturbation theory for small V_{nn} : $K_f = 1 + \frac{V_{\text{nn}}(1-\cos 2k_F)}{2\pi \sin k_F}$, $u_f = 2J \sin k_F \left(1 - \frac{V_{\text{nn}}(1-\cos 2k_F)}{2\pi J \sin k_F} \right)$.

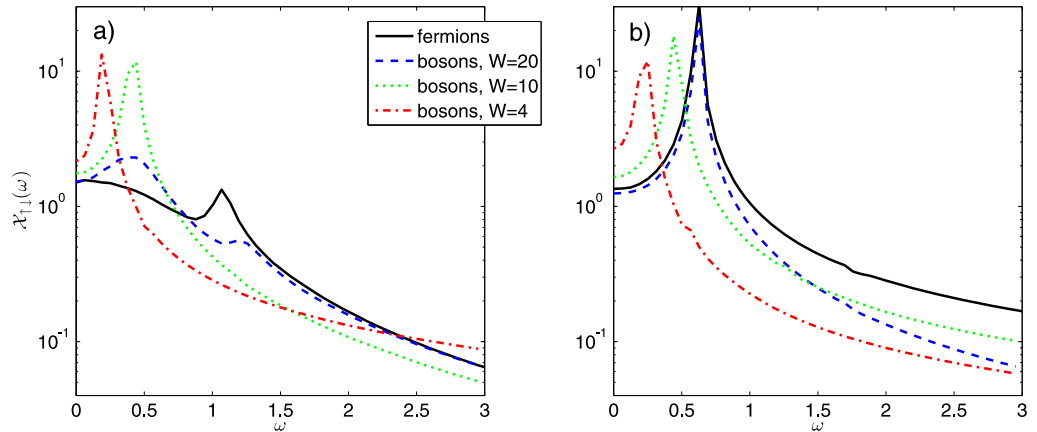


Figure 14. Comparison of $\mathcal{X}_{\uparrow\downarrow}(\omega)$ between fermions and bosons in the strong-attraction case, $|U|/J = 10$. (a) $N_{\uparrow} = 140$. For the fermion bath (black solid line), the virtual pair-breaking peak (cf section 2.2) has become dominant, with the doublon peak at lower frequency having almost completely flattened out. For bosons at $W/J = 20$ (blue dashed line), the behaviour is qualitatively similar, but the oscillation of the doublon is still dominant, as evidenced by the larger low-frequency peak. For $W/J = 10$ (green dotted line) and $W/J = 4$ (red dash-dotted line), only the high-order bound states oscillate; there is no virtual pair-breaking peak. (b) $N_{\uparrow} = 180$. For the fermion bath, the virtual pair-breaking peak (cf section 2.2) is now fully dominant, with the doublon peak at lower frequency having completely vanished. The dynamics for the boson bath at $W/J = 20$ (blue dashed line) now almost completely matches that of the fermions, showing that for bosons as well a virtual pair-breaking peak, corresponding to the fermionization of the bosonic gas. For $W/J = 10$ and 4, only the high-order bound states oscillate as in (a); there is again no virtual pair-breaking peak.

Computing K_b and u_b for densities between 0 and 0.2 and large W/J shows that equation (17) can be read equivalently as the model of an impurity coupled to weakly nearest-neighbour attractive spinless fermions. For example, for $W/J = 10$ and $n_{\uparrow} = 0.1$, $K_b = 1.039$, $u_b/J = 0.59$, values that are best matched by K_f and u_f for $|V|/J = 0.75$, $k_F = 0.1\pi$. Crucially, a value of $K_f = 1.039$ is still very close to the values for free fermions, $K_f = 1$. Thus, the continued applicability of equation (14)—which had initially been developed from a one-body picture of the free fermion bath—to predict the polaron peak in the weak-coupling regime even for a (sufficiently repulsive) bosonic bath can be explained (cf figure 13).

3.2. The strong interaction limit—higher-order bound states of the impurity

In the opposite limit of large bath–impurity attraction, $|U| \gg J$, the kick-induced dynamics of the impurity start to depend crucially on the ratio $|U|/W$. As an example, as for the fermions, we focused on the case $|U|/J = 10$. As long as $W > |U|$, the spectrum of doublon dynamics, $\mathcal{X}_{\uparrow\downarrow}(\omega)$, remains qualitatively unaltered from the case of the fermionic bath: when $n_{\uparrow} < 0.5$, the dynamics of the kicked impurity are dominated by the oscillation of the doublon mode,

Table 1. Table summarizing the different regimes identified for the problem considered here.

$ U $ range	Bath population	Dynamics regime
Strong interaction	Large N_{\uparrow}	Free particle
Strong interaction	Intermediate N_{\uparrow}	Bound pair + polaron internal dynamics
Strong interaction	Small N_{\uparrow}	Bound pair
Weak interaction	Large N_{\uparrow}	Free particle
Weak interaction	Intermediate and small N_{\uparrow}	Free particle + polaron

whereas for $n_{\uparrow} \geq 0.5$ this doublon peak increasingly flattens out and eventually disappears as n_{\uparrow} increases above half-filling, as shown in figure 14. At the same time, like for fermions, a high-frequency peak appears for $n_{\uparrow} \geq 0.5$, increasing in amplitude as n_{\uparrow} grows above the threshold while the doublon peak decreases, signalling the transition of the dynamics to a regime dominated by the virtual breaking of the pair (cf section 2.2). Even for a substantial value of W , $W/J = 20$, the value of the oscillation frequency is higher than in the fermionic case, signalling an incomplete transition to a Tonks regime for the bosonic system.

On the other hand, when the boson–boson repulsion W becomes comparable to or smaller than the magnitude of the boson–impurity attraction $|U|$, the numerics clearly show that higher-order bound states between the impurity and the bath particles are formed in the ground state. At $W/J = |U|/J = 10$, both doublon and trion states (the impurity binding to one or two bath particles on-site, respectively) are present, whereas for $W/J = 4$, doublon, trion and quatrimon bound states are occupied, with the trion state carrying the largest weight at any bath density. When quasi-momentum is applied to the impurity by the kick, these higher-order bound states perform oscillations, at frequencies significantly lower than those for the doublons due to the even higher effective mass. Interestingly, the damping we observe becomes gradually smaller, the smaller the W/J is, with the oscillations at $W/J = 4$ showing almost no decay at any value of n_{\uparrow} in the time domain over which we simulate. An interesting question for further study is whether this effect is due to the partial ability of 1D superfluids to be protected against excitations [29, 57]—which would be the source of a damping of the bound state oscillations.

4. Discussion and conclusions

The dynamics of an impurity moving on a 1D lattice inside a fermionic bath, or a strongly repulsive bosonic one, shows intriguingly complex dynamics, as can be seen by studying the time evolution of the doublon density. One of the characteristic frequencies that appear corresponds to the motion of a free particle, appearing in the limit of high filling of the bath, and is easily understood due to the increasingly uniform interaction energy the impurity experiences on all the sites. Another feature of the dynamics, namely the oscillations of a bound pair are also rather intuitive to understand, allows us to draw an analogy with the molecule versus polaron question in 3D continuum systems. The bound pair is present in the regime of large $|U|/J$ and low density, like the molecule in the polaron versus molecule analogy. In the limit of small $|U|/J$, we observed the dynamics of a free particle side-by-side pair breaking of the correlated states of a polaron. This actually corresponds well to the

polaron ansatz [12], which is a superposition of a non-interacting Fermi sea (free particle) plus a contribution from correlated particle–hole states. Thus, the crossover from a polaron to a bound pair with increasing interaction is also taking place in analogy with higher dimensional continuum systems. In our system, however, we have a feature that does not have any analogy in the polaron versus molecule crossover in 3D continuum, namely the high-frequency peak in the large $|U| = J$ regime, which becomes dominant for bath fillings above 0.5, which is the result of a virtual particle–hole creation process. This virtual exchange of paired and bath particles can be read as a kind of internal dynamics of the polaron. Observation of the dynamics predicted here should be feasible in currently available ultracold gases systems, provided that the temperature is below the energy scale of the oscillations, which we found to be of the order of $0.1J-1J$.

Acknowledgments

We thank J Kajala for useful discussions. This work was supported by the Academy of Finland through its Centres of Excellence Programme (project numbers 251748, 263347, 135000 and 141039), by ERC (grant number 240362-Heatronics) and by the Swiss NSF under MaNEP and Division II. Work in Pittsburgh is supported by the NSF under grant number PHY-1148957. Computing resources were provided by the Finnish IT Centre for Science, CSC.

Appendix

A.1. Effective mass from the Bethe ansatz

We show here how to gain some insight into the problem through the string hypothesis for the solution of the Lieb–Wu equations whose solutions describe (most of) the eigenvalues of the Hubbard Hamiltonian in one dimension (chapter 4 of [30]), in the limit of large lattice lengths L . For a fixed total number of particles N and the number of down particles M , the patterns that the solutions of the Lieb–Wu equations are composed of can be classified into three different categories:

- $k - \Lambda$ strings;
- single real values of k_j ;
- Λ strings.

Every eigenstate of the Hubbard Hamiltonian can be represented in terms of a particular configuration of strings, containing M_n Λ -strings, $M'_n k - \Lambda$ strings of length n (in our case $n = 1$) and \mathcal{M}_e single k_j . Here M_n, M'_n, \mathcal{M}_e are related to N and M by

$$M = \sum_{n=1}^{\infty} n (M_n + M'_n), \quad (\text{A.1})$$

$$N = \mathcal{M}_e + \sum_{n=1}^{\infty} 2n M'_n. \quad (\text{A.2})$$

In our case, $M = 1$ implies the existence of two classes of string solutions:

- (A) $M_n = 1, M'_n = 0, \mathcal{M}_e = L$: this solution is characterized by one Λ string composed of a single real value, N real k_j s and no $k - \Lambda$ strings.
- (B) $M_n = 0, M'_n = 1, \mathcal{M}_e = L - 2$: in this case the solution is characterized by $N - 2$ real k_j s and one $k - \Lambda$ string, characterized by two (complex valued) $k_{1,2}$ s and one real Λ , related by

$$\sin(k_{1,2}) = \Lambda \pm iU/4J. \quad (\text{A.3})$$

In terms of the string parameters, the energy and quasi-momentum are given by

$$P = \left[\sum_{j=1}^{N-2M'} k_j - \sum_{n=1}^{\infty} \sum_{\alpha=1}^{M'_n} (2 \operatorname{Re} \arcsin (\Lambda'_{\alpha}{}^n + niU/4J) - (n+1)\pi) \right] \bmod 2\pi, \quad (\text{A.4})$$

$$E = -2J \sum_{j=1}^{N-2M'} \cos(k_j) + 4J \sum_{n=1}^{\infty} \sum_{\alpha=1}^{M'_n} \operatorname{Re} \sqrt{1 - (\Lambda'_{\alpha}{}^n + niU/4J)^2}. \quad (\text{A.5})$$

The two classes of solutions identified previously, see appendices A and B above, take the following form:

$$(A) \quad P = \sum_{j=1}^N k_j, \quad (\text{A.6})$$

$$E = -2J \sum_{j=1}^N \cos(k_j) + \text{const.} \quad (\text{A.7})$$

$$(B) \quad P = \sum_{j=1}^{N-1} k_j - 2 \operatorname{Re} [\arcsin (\Lambda + iU/4J)], \quad (\text{A.8})$$

$$E = -2J \sum_j^{N-1} \cos(k_j) + 4J \operatorname{Re} \sqrt{1 - (\Lambda + iU/4J)^2} + \text{const.} \quad (\text{A.9})$$

The solution containing the $k - \Lambda$ string can be written in a more transparent form as

$$P = \sum_{j=1}^{N-1} k_j + 2q, \quad (\text{A.10})$$

$$E = -2J \sum_j^{N-1} \cos(k_j) - 4J \cosh \xi \cos(q) + \text{const.}, \quad (\text{A.11})$$

where $q = \operatorname{Re}[k_1] = \operatorname{Re}[k_2]$ and $\xi = \operatorname{Im}[k_1] = -\operatorname{Im}[k_2]$, with k_1 and k_2 belonging to the $k - \Lambda$ string. For the $k - \Lambda$ string it is possible to prove (see [30, p 134]) that

$$\cosh \xi = \sqrt{1 + \frac{U^2}{16J^2 \cos^2(q)}}. \quad (\text{A.12})$$

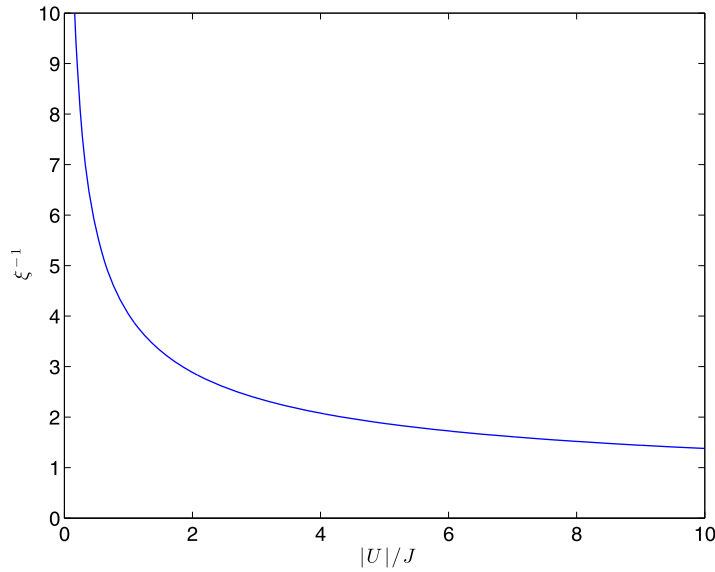


Figure A.1. The pair size (ξ^{-1}) as a function of U .

From the form of the wavefunction associated with the $k - \Lambda$ string, ξ describes the (exponential) spatial decay of the pair, and thus ξ^{-1} can be interpreted as the size of the pair.

In the strongly interacting limit we have

$$-4J \cosh \xi \cos q \rightarrow U - 4J^2/|U| - 4J^2/|U| \cos(2q) + O\left(\frac{1}{U^2}\right), \quad (\text{A.13})$$

which is coherent with the strong-coupling calculation leading to the Heisenberg Hamiltonian for the Hubbard Hamiltonian in the strong-coupling limit (modulo a $U \rightarrow -U$ mapping).

The spectrum is thus composed of a lower band ($k - \Lambda +$ single ks solutions) and a higher band (single ks and single Λ solutions). Intuitively, the former corresponds to a pair in an unpaired background Fermi sea, whereas the latter corresponds to scattering states. The down particle which is kicked in our simulations, with a view to the collective nature of the excitations in 1D systems, can be considered as composed of both kinds of elementary excitations, appropriately weighted by the presence of the trapping potential.

We now aim at describing the dynamics that we observed numerically through the evaluation of the effective mass for the pairs

$$m_{\text{doublon}} = \left(\frac{\partial^2 E}{\partial \kappa^2} \right)^{-1} \Big|_{\kappa=0} \quad (\text{A.14})$$

$$= \frac{1}{J} \sqrt{1 + \frac{U^2}{16J^2}}, \quad (\text{A.15})$$

where E is defined by equation (A.10).

A.2. The frequency of the non-interacting particle in the combined harmonic trap and lattice potential

The idea is to compare the oscillation frequency from the numerical data to that given by the non-interacting particle in a combined lattice and harmonic trap potential. As a reminder, the

formula for the centre-of-mass position was given by

$$\langle x \rangle = \delta \exp \left[\left(\frac{\delta}{a_{\text{ho}}} \right)^2 \sin^2 (V/8t) \right] \cos \left[V \left(\sqrt{\frac{2}{Vm_{\text{eff}}}} - \frac{1}{4} \right) t - \frac{\delta^2}{2a_{\text{ho}}^2} \sin \left(\frac{Vt}{4} \right) + \frac{\pi}{2} \right]. \quad (\text{A.16})$$

Neglecting the exponential prefactor time dependence, we can write the centre-of-mass oscillation frequency as

$$\omega_{\text{COM}} = \frac{d\Omega}{dt}, \quad (\text{A.17})$$

where

$$\Omega = V \left(\sqrt{\frac{2}{Vm_{\text{eff}}}} - \frac{1}{4} \right) t - \left(\frac{\delta}{a_{\text{ho}}} \right)^2 \sin \left(\frac{Vt}{4} \right) + \frac{\pi}{2}$$

with $\delta = \left[\frac{(1-\cos k)}{Vm_{\text{eff}}} - \frac{1}{16} - \frac{\sqrt{V/J}}{256} \right]^{1/2}$, leading to

$$\omega_{\text{COM}} = V \left[\left(\sqrt{\frac{2}{m_{\text{eff}}V}} - \frac{1}{4} \right) - \frac{\sqrt{V/J}}{4} \left(\frac{1-\cos k}{m_{\text{eff}}V} - \frac{1}{16} - \frac{\sqrt{V/J}}{256} \right) \right]. \quad (\text{A.18})$$

The comparison between ω_{COM} and the numerical data is obtained by performing a discrete Fourier transform of $\langle n_{\uparrow} n_{\downarrow} \rangle(t)$ for different values of U and N_{\uparrow} . For $N_{\uparrow} = N_{\downarrow} = 1$, i.e. no bath, the agreement is perfect: higher interaction energies correspond to lower values of the oscillation frequency, in agreement with the increase of the effective mass.

References

- [1] Mahan G D 2010 *Many Particle Physics* (Berlin: Springer) (softcover reprint of the hardcover 3rd edn of 2000)
- [2] Kondo J 1964 *Prog. Theor. Phys.* **32** 37
- [3] Lee P A and Wen X-G 2006 *Rev. Mod. Phys.* **78** 17
- [4] Ketterle W, Inouye S, Andrews M R, Stenger J, Miesner H J and Stamper-Kurn D M 1998 *Nature* **392** 151
- [5] Bloch I, Dalibard J and Zwierger W 2008 *Rev. Mod. Phys.* **80** 885
- [6] Schirotzek A, Wu C-H, Sommer A and Zwierlein M W 2009 *Phys. Rev. Lett.* **102** 230402
- [7] Nascimbène S, Navon N, Jiang K J, Tarruell L, Teichmann M, McKeever J, Chevy F and Salomon C 2009 *Phys. Rev. Lett.* **103** 170402
- [8] Sommer A, Ku M and Zwierlein M W 2011 *New J. Phys.* **13** 055009
- [9] Koschorreck M, Pertot D, Vogt E, Fröhlich B, Feld M and Köhl M 2012 *Nature* **485** 619
- [10] Kohstall C, Zaccanti M, Jag M, Trenkwalder A, Massignan P, Bruun G M, Schreck F and Grimm R 2012 *Nature* **485** 615
- [11] Zhang Y, Ong W, Arakelyan I and Thomas J 2012 *Phys. Rev. Lett.* **108** 235302
- [12] Chevy F 2006 *Phys. Rev. A* **74** 063628
- [13] Prokofév N and Svistunov B 2008 *Phys. Rev. B* **77** 125101
- [14] Massignan P, Bruun G and Stoof H 2008 *Phys. Rev. A* **78** 031602
- [15] Punk M, Dumitrescu P and Zwierger W 2009 *Phys. Rev. A* **80** 053605
- [16] Zöllner S, Bruun G and Pethick C 2011 *Phys. Rev. A* **83** 021603
- [17] Parish M 2011 *Phys. Rev. A* **83** 051603
- [18] Massignan P and Bruun G M 2011 *Eur. Phys. J. D* **65** 83
- [19] Giraud S and Combescot R 2012 *Phys. Rev. A* **85** 013605

- [20] Schmidt R, Enss T, Pietilä V and Demler E 2012 *Phys. Rev. A* **85** 021602
- [21] Baarsma J, Armatitis J, Duine R and Stoof H T 2012 *Phys. Rev. A* **85** 033631
- [22] Ngampruetikorn V, Levinsen J and Parish M M 2012 *Europhys. Lett.* **98** 30005
- [23] Knap M, Shashi A, Nishida Y, Imambekov A, Abanin D A and Demler E 2012 arXiv:1206.4962
- [24] Zvonarev M B, Cheianov V V and Giamarchi T 2007 *Phys. Rev. Lett.* **99** 240404
- [25] Zvonarev M B, Cheianov V V and Giamarchi T 2009 *Phys. Rev. Lett.* **103** 110401
- [26] Zvonarev M B, Cheianov V V and Giamarchi T 2009 *Phys. Rev. B* **80** 201102
- [27] Imambekov A and Glazman L I 2008 *Phys. Rev. Lett.* **100** 206805
- [28] Lamacraft A 2009 *Phys. Rev. B* **79** 241105
- [29] Giamarchi T 2003 *Quantum Physics in One Dimension* (Oxford: Clarendon)
- [30] Essler F H L, Frahm H, Göhmann F, Klümper A and Korepin V E 2005 *The One-Dimensional Hubbard Model* (Cambridge: Cambridge University Press)
- [31] Leskinen M, Nummi O, Massel F and Törmä P 2010 *New J. Phys.* **12** 073044
- [32] Guan X W 2012 *Front. Phys.* **7** 8
- [33] Mathy C J M, Zvonarev M B and Demler E 2012 arXiv:1203.4819
- [34] Schechter M, Kamenev A, Gangardt D and Lamacraft A 2012 *Phys. Rev. Lett.* **108** 207001
- [35] Palzer S, Zipkes C, Sias C and Köhl M 2009 *Phys. Rev. Lett.* **103** 150601
- [36] Catani J, Lamporesi G, Naik D, Gring M, Inguscio M, Minardi F, Kantian A and Giamarchi T 2012 *Phys. Rev. A* **85** 023623
- [37] Peotta S, Rossini D, Polini M, Minardi F and Fazio R 2012 arXiv:1206.3984
- [38] Bonart J and Cugliandolo L F 2012 *Phys. Rev. A* **86** 023636
- [39] Bakr W S, Peng A, Tai M E, Ma R, Simon J, Gillen J I, Folling S, Pollet L and Greiner M 2010 *Science* **329** 547
- [40] Sherson J F, Weitenberg C, Endres M, Cheneau M, Bloch I and Kuhr S 2010 *Nature* **467** 68
- [41] Fukuhara T *et al* 2012 arXiv:1209.6468
- [42] Vidal G 2004 *Phys. Rev. Lett.* **93** 040502
- [43] Daley A J, Kollath C, Schollwoeck U and Vidal G 2004 *J. Stat. Mech.* P04005
- [44] White S R and Feiguin A E 2004 *Phys. Rev. Lett.* **93** 076401
- [45] Verstraete F, Murg V and Cirac J J I 2008 *J. Stat. Mech.* **57** 143
- [46] Massel F, Leskinen M J and Törmä P 2009 *Phys. Rev. Lett.* **103** 066404
- [47] Korolyuk A, Massel F and Törmä P 2010 *Phys. Rev. Lett.* **104** 236402
- [48] Kajala J, Massel F and Törmä P 2011 *Phys. Rev. Lett.* **106** 206401
- [49] Kajala J, Massel F and Törmä P 2011 *Phys. Rev. A* **84** 041601
- [50] Rey A, Pupillo G, Clark C and Williams C 2005 *Phys. Rev. A* **72** 033616
- [51] Winkler K, Thalhammer G, Lang F, Grimm R, Denschlag J H, Daley A J, Kantian A, Büchler H and Zoller P 2006 *Nature* **441** 853
- [52] Valiente M and Petrosyan D 2008 *J. Phys. B: At. Mol. Opt. Phys.* **41** 161002
- [53] Matveev K, Yue D and Glazman L 1993 *Phys. Rev. Lett.* **71** 3351
- [54] Fabrizio M and Gogolin A O 1995 *Phys. Rev. B* **51** 17827
- [55] Friedel J 1958 *Nuovo Cimento* **7** 287
- [56] Cazallila M A, Citro R, Giamarchi T, Orignac E and Rigol M 2011 *Rev. Mod. Phys.* **83** 1405
- [57] Kane C and Fisher M 1992 *Phys. Rev. Lett.* **68** 1220